Enhanced Field Emission Properties of α-Fe2O3 Nanostructures with the Removal of Adsorbed Gas Molecules

4 AUTHORS, INCLUDING:

Junpeng Lu
National University of Singapore
25 PUBLICATIONS **140** CITATIONS

SEE PROFILE

Minrui Zheng
National University of Singapore
**32** PUBLICATIONS **278** CITATIONS

SEE PROFILE

Enhanced Field Emission Properties of α-Fe₂O₃ Nanostructures with the Removal of Adsorbed Gas Molecules

Lu Junpeng,[†] Yun Tao,[†] Zheng Minrui,[†] and Sow Chorng Haur[†],*

[†]Department of Physics, 2 Science Drive 3, National University of Singapore (NUS), Singapore-117542.

S *Supporting Information*

ABSTRACT: Quasi-1D α-Fe₂O₃ nanostructure arrays of four different morphologies (random nanoflakes, random nanobelts, quasi-aligned nanostrips and quasi-aligned nanoneedles) were successfully synthesized via a simple heating process. Field emission measurements indicate that the α-Fe₂O₃ nanoneedle arrays are superior field emitter exhibiting low turn-on voltage, high current density, and large field-enhancement factor due to better vertical alignment and higher aspect ratio. In addition, we found that adsorbed oxygen molecules greatly hindered the field emission performance of the nanostructures. Prolonged field emission process could drive the oxygen molecules away and give rise to markedly improved and efficient α-Fe₂O₃ nanostructures field emitter. The improved field emission is attributed to desorption of the oxygen molecules during the field emission process.
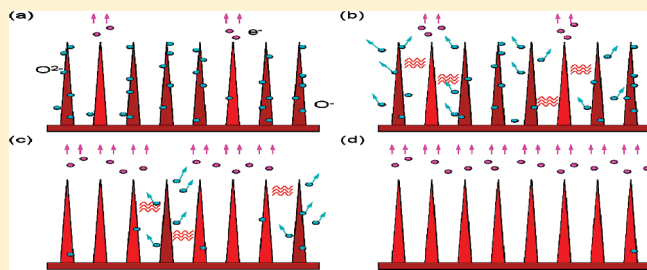
1. INTRODUCTION

Quasi-1D nanostructures such as nanotubes, nanowires, and nanobelts have attracted great attention due to their promising properties which can be applied in fabrication of novel electronic, magneto-electronic, photoelectronic, and electromechanical nanodevices,[1,2] such as field-effect transistors,[3] memory cell,[4] solar cells,[5] and piezo nanogenerators.[6,7] With sharp tips and high aspect ratio, 1D nanostructures are promising candidates for field emission displays[8] as field emitter to yield electron source with high brightness. Among these 1D nanomaterials, field emission properties (FE) of carbon nanotubes, ZnO, CuO, ZnS nanowires,[9−12] and so forth, have been extensively studied recently and the fabrication of field emission devices based on these materials has also been explored.[13]

α-Fe₂O₃ (hematite), a semiconductor material with a band gap of 2.1 eV, acting as the most stable state among iron oxides under ambient condition, has been widely studied in recent years.[14−16] There exist various methods to synthesize α-Fe₂O₃ quasi-1D nanostructures, including template assisted methods,[17] thermal evaporation,[18] hydrothermal reaction,[19] and direct thermal oxidation.[20] Direct thermal oxidation is a promising approach that can be used to fabricate high quality 1D nanostructure and therefore interested several research groups. For example, Fu et al.[21] synthesized α-Fe₂O₃ nanowire arrays through oxidation of iron foil in a special oxidizing mixture gases including 19.30% CO_2, 0.14% SO_2, 80.56% NO_2, and some H_2O. Hsu et al.[22] fabricated α-Fe₂O₃ nanowires through thermal oxidation of an iron layer coated on an ITO glass by RF sputtering and studied their field emission property. More recently our group reported a simple and efficient approach to synthesize α-Fe₂O₃ nanoflakes by heating iron foil on a hot plate in air.[23] And we managed to fabricate aligned α-Fe₂O₃

nanoflakes arrays on an AFM tip using this method and studied their field emission properties.[24] These studies indicate the potential application of α-Fe₂O₃ 1D nanostructures as field emitter. However, the FE turn-on field is still as high as 12.5 V/μm[25] which might limit the FE performance of α-Fe₂O₃ nanostructure. In this article, we extended our work of synthesis of α-Fe₂O₃ nanostructure by extending the growth temperature to a wider range. With this, we managed to synthesize four kinds of α-Fe₂O₃ 1D nanostructures with different morphologies, nanoflakes (sample A), random nanobelts (sample B), nanostrips (sample C), and nanoneedles (sample D). Each of these samples was created by direct thermal oxidation of an iron foil, which acted as both precursor and substrate. Using these nanomaterials as FE emitter, very low turn-on field, low threshold field, and high current density were achieved.

Up until now, research scientists continuously try to find promising quasi-1D materials with sufficiently low work function and suitable morphologies as potential field emitters. In previous reported studies on field emission performance, most of the research groups focused their attention on the intrinsic properties, such as work function, crystal structures, and emitter morphologies, which include aspect ratios, emitter density, and spatial distribution of emitting center of the nanomaterials.[26] For example, Zhao et al.[27] treated AlN nanorods in different thermal annealing conditions to increase their crystal quality and reduce work function, and therefore investigated these effects on the field emission properties. In our previous work, Rakhi et al.[28] encapsulated magnetic nanomaterials into multiwalled carbon

nanotubes and demonstrated the improvement of field emission arising from the decrease of the effective work function compared with pure carbon nanotubes or those magnetic nanomaterials. About the morphologies effects, Pan et al.[29] reported the effect of carbon nanotube morphology on field emission properties. More recently, Zhai et al.[30] synthesized CdS nanostructure arrays with different ordered alignment and discussed the enhancement of field emission from vertical alignment. Among the many studies on field emission, only a few researchers pay attention to the influence of external factors (such as humidity, gas pressure, and residual gas). In 1996, Chernozatons et al.[31] reported the influence of residual gas pressure and temperature on the field emission of carbon nanotubes. In 2004, Chen et al.[32] studied the single-walled carbon nanotube FE behavior under the influence of adsorbates. They found some gas molecules enhanced FE through the lowering of the work function, whereas some gas molecules degraded the FE through the creation of blunt tips. Notably, fewer people took notice of the lingering influence of the adsorbed gas molecules that were anchored onto the surface of the 1D nanostructure despite the fact that the chamber was pumped to a high vacuum. To the best of our knowledge, the effect of adsorbed gas molecules of the FE performance of α-Fe$_2$O$_3$ nanostructure has not been reported before. In the second part of this work, the effect of the gas molecules adsorption on the FE performance of α-Fe$_2$O$_3$ nanoneedles was thoroughly studied. We observed a huge influence caused by adsorption of oxygen molecules on the well-aligned 1D α-Fe$_2$O$_3$ nanoneedles (sample D) and have demonstrated the mechanism of this kind of effects. Hundred times enhancement of emission current density were obtained after the removed of these adsorbed oxygen molecules through a simple in situ method. Namely, this was achieved by applying electric field to the field emitters repeatedly. Therefore, this work could put forward a reminder that 1D electron field emitter should operate under high vacuum and much better performance could potentially be obtained after prior treatment of the nanostructure using the same FE setup.

2. EXPERIMENTAL SECTION

Commercial iron foils (10 × 10 × 0.1 mm) with a purity of 99.99% (Alfa Aesar) were used as the heating targets for the growth of α-Fe$_2$O$_3$ nanostructures. The Fe foils were polished with sandpaper and cleaned with isopropanol. For the synthesis of α-Fe$_2$O$_3$ nanoflakes (sample A), a treated Fe foil was heated on a thermal hot plate under ambient conditions, the same as our previous work.[23] Maroonlike products were observed after the foil was heated to a temperature of 350 °C for 10 h. To synthesize the nanobelts (sample B), an Fe foil was initially heated to 700 °C in a vacuum chamber of a Plasma Enhanced Chemical Vapor Deposition (PECVD) system under a low pressure environment of about 1×10^{-6} Torr. Oxygen was allowed to flow into the chamber at a rate of 30 sccm. During growth, the duration and pressure inside the chamber were fixed at 4 h and 1 Torr, respectively, while an oxygen plasma was created with a radio frequency (RF) power of 100 W in the chamber. The α-Fe$_2$O$_3$ nanostrips (sample C) and nanoneedles (sample D) were synthesized through heating Fe foils inside a small tube furnace with a length of 30 cm at atmospheric environment. The growth temperature was fixed at 750 and 800 °C respectively for 4 h. After cooling down to room temperature, dull-red, and bright-red products were observed, respectively.

The morphologies of these products were studied using a scanning electron microscope (SEM, JEOL JSM-6700F). Structural details were characterized by X-ray diffraction (XRD, Phillips PW 127) and a micro-Raman system (Renishaw System 2000, 514 nm excitation). A transmission electron microscope (TEM, JEOL JEM-2010F) was used to examine detailed morphology and crystalline order of the nanostructures. The field emission (FE) measurements were carried out in a closed chamber with a low pressure of about 5×10^{-7} Torr under a two-parallel-plate setup.[11] The as-prepared nanostructure arrays were attached onto a copper substrate cathode through copper double-side tape. A piece of ITO glass coated with a layer of phosphor acted as the anode. The gap distance was kept at 100 or 200 μm between two electrodes. A voltage from 0 to 1100 V was applied and the emission current was measured at the same time using a Keithley 237 high-voltage source measure unit. All of the measurements were carried out at room temperature.

3. RESULTS AND DISCUSSION

After each synthesis run, optical pictures of these samples were captured. Part a of Figure 1 shows samples A, B, C, and D from upper left to bottom right. The maroon colored sample A was heated on the hot plate at 350 °C for 10 h. Samples grown in PECVD resulted in mottled dark-red products (sample B). The foils grown in tube furnace at 750 °C (sample C) and 800 °C (sample D) show uniform dark-red (part c of Figure 1) and bright-red (part d of Figure 1) colors. These samples were observed in SEM to examine the influences of different parameters on the growth of nanostructures. Sample A exhibits random ordered nanoflakes (part b of Figure 1) with widths of about 150−200 nm at the bases, 30 nm at the tips, and 3−5 μm of length. Part c of Figure 1 shows the SEM image of sample B, comprised of random nanobelts, with widths of about 500 nm at the bottom, terminated with long, etched tips and 3−13 μm in length, disorderedly distributed on the substrate. The zigzaglike edges may be caused by plasma gas turbulence resulted from oxygen gas introduced into or out of the chamber.[33] As can be seen from the insert of part c of Figure 1, some part of the substrate showed low coverage of nanobelts, in accordance with the case of mottled optical image part a of Figure 1. Sample with lower nanobelts density may show improved field emission enhancement factor but it will suffer from nonuniform electron emission. Part d of Figure 1 reveals the morphology of sample C, which consists of more vertical aligned nanostrips, which are about 50 nm in thickness, 300 nm in width, and about 10 μm in length, occasionally showing sharp tips. When heating at a little higher temperature, the products, sample D, would be nanoneedles, as shown in part e of Figure 1. They are about 70 nm in diameter and 10−20 μm in length with decreasing width from the bottom to the top and terminate with an ultra sharp tip. Part f of Figure 1 shows the tilted 45° view of sample D. We can see the nanoneedles are more vertically aligned. It should be noted that within the heating range of 400−700 °C, we did not observe the growth of nanostructures, the SEM images of samples heatd in this range are shown in Figure S1 of the Supporting Information. Therefore, we introduced oxygen plasma at 700 °C to induce nanostructure growth in the case of sample B. A summary of the parameters including morphology, aspect ratio (L/FWHL, L is the length and FWHL is full width of half length), density, FE performance characteristics for these samples are listed in the Table 1.

8817

dx.doi.org/10.1021/jp200858g |J. Phys. Chem. C 2011, 115, 8816–8824

The micro-Raman spectra of these as-grown products, recorded at room temperature, are shown in Figure 2. These four samples exhibited similar Raman spectra. In the range of 200–1500 cm^{-1}, there are six narrow bands at 226, 247, 293, 411, 499, and 613 cm^{-1}, namely four E_{1g} modes (247, 293, 411, and 613 cm^{-1}) and two A_{1g} modes (226 and 499 cm^{-1}), and a distinct peak at 1318 cm^{-1}. All of these peak positions are in agreement with previous results,[34] corresponding to the rhombohedral α-Fe$_2$O$_3$ phase.[35]

The X-ray diffraction (XRD) patterns of these α-Fe$_2$O$_3$ nanostructures are shown in Figure 3. Evidently, two kinds of

iron oxide phase peaks, α-Fe$_2$O$_3$ and Fe$_3$O$_4$, are present in sample A, which identifies with the growth mechanism that we reported previously.[23] However, with the increase in growth temperature, only the peaks indicating pure α-Fe$_2$O$_3$ phase (rhombohedral structure) are left. When the temperature exceeded 750 °C, for sample C and D, the (110) peak at 35.2° is dominant, resulting from the vertical alignment of the nanostructures grown along the [110] direction. This case is due to the homoepitaxial growth mechanism. As mentioned above, when the temperature was kept between 400 and 700 °C, no 1D nanostructure was formed. Only a moltenlike layer was found on the substrate surface shown in Figure S1 of the Supporting
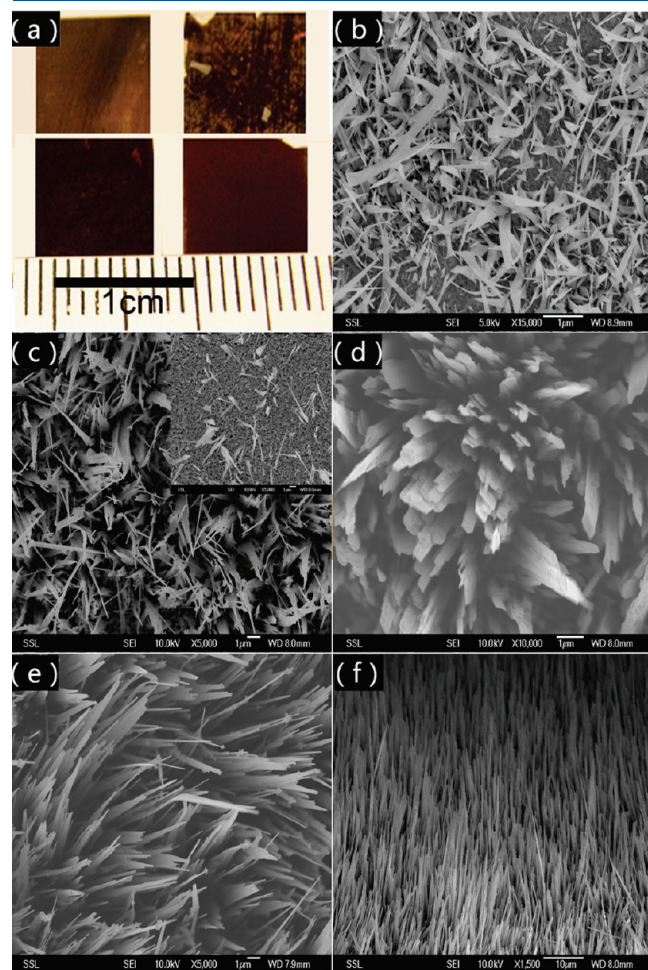

Figure 1. (a) Optical images of four kinds of different morphologies α-Fe$_2$O$_3$ nanostructures. From top left to right and bottom left to right are sample A, sample B, sample C, and sample D. And SEM images of α-Fe$_2$O$_3$ nanostructures: (b) sample A, (c) Top view of sample B, the insert of (c) shows the nonuniform and low density of sample B, (d) sample C, (e) sample D, and (f) the side view of sample D, revealing the more vertical alignment of the nanoneedles.
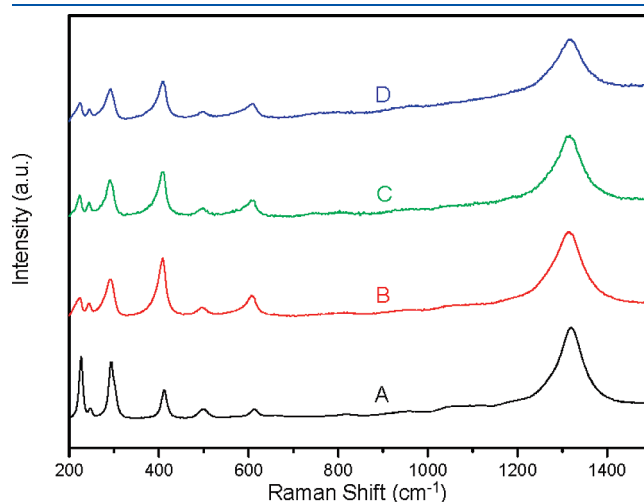

Figure 2. Raman spectra of as-prepared samples A, B, C, and D. All of these peaks are corresponding to rhombohedral α-Fe$_2$O$_3$ phase.

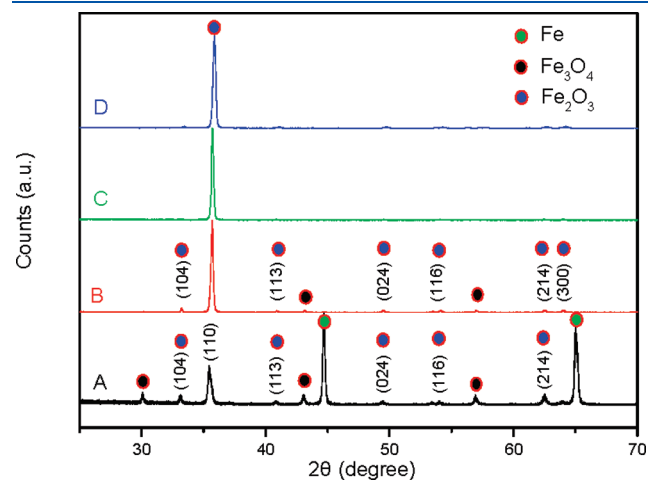**Figure 3.** XRD pattern of the as-prepared α-Fe$_2$O$_3$ nanostructures (samples A, B, C, and D).

Table 1. Morphology Description and Turn-On Field, Threshold Field, β of Four As-Prepared α-Fe$_2$O$_3$ Nanostructure Arrays

samples	morphology	aspect ratio	density (number/μm^2)	turn-on field (V/μm)	threshold field (V/μm)	β
A	randomly ordered nanoflakes arrays	40	18.42	10.35		537
B	randomly ordered nanobelts arrays	20	dense area:1.81 sparse area:0.25	5.05	10.7	4774
C	quasi-aligned nanostrips arrays	33	1.46	3.75	7.3	3292
D	quasi-aligned nanoneedles arrays	230	1.5	1.7	2.83	5310

Information. From Raman spectrum and XRD pattern in Figures S2 and S3 of the Supporting Information, this layer is α-Fe_2O_3. Therefore, for the growth of α-Fe_2O_3 nanostructures at temperatures that exceed 750 °C, we have the pleasant advantage of the promotion of preferential growth of aligned α-Fe_2O_3 nanostructures.
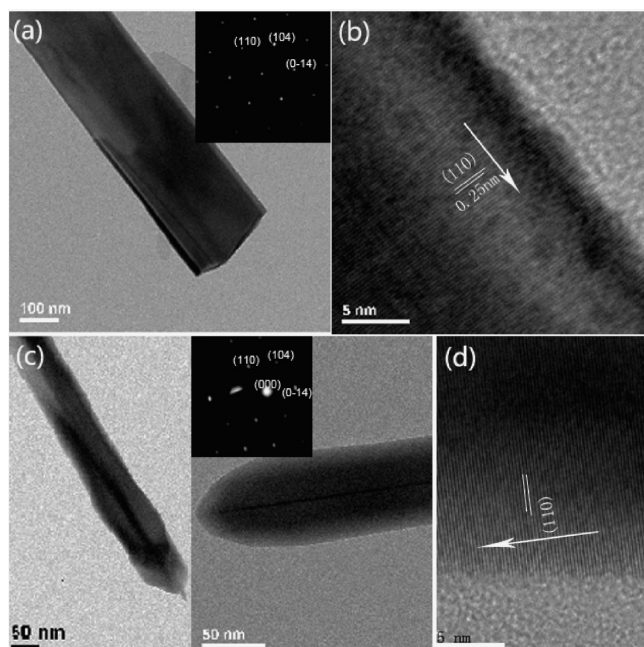

Figure 4. (a) TEM and (b) HRTEM images of a single α-Fe_2O_3 nanostrip (sample C), insert of panel (a) shows the SAED pattern. (c) TEM and (d) HRTEM images of a single α-Fe_2O_3 nanoneedle (sample D), insert of (c) shows the SAED pattern.

The detailed microstructures of these nearly vertically aligned α-Fe_2O_3 nanostructures were further studied by transmission electron microscopy (TEM). Part a of Figure 4 shows a typical TEM image of sample C. The corresponding selected area electron diffraction (SAED) pattern of the nanostrip, shown in the insert, indicated the growth direction of the nanostrip to be [110]. The high-resolution TEM (HRTEM) image shown in part b of Figure 4 revealed the nanostrip to be single crystalline and the fringe spacing between adjacent lattice planes was measured to be 0.252 nm corresponding to the (110) interplanar distance. Typical TEM image of sample D is shown in part c of Figure 4. The nanoneedles possess a radius of about 70 nm and a sharply thin tip formed on the top. Both the SAED pattern shown in the insert and the HRTEM shown in part d of Figure 4 indicate the growth direction of the nanoneedles to be [110], namely, c axis is the dominant growth axis.

Field-emission (FE) studies showed that the α-Fe_2O_3 nanostructures are effective field emitters. Up until now, the studies on the field-emission (FE) properties of α-Fe_2O_3 nanostructures have been rather limited compared to other nanomaterials such as CuO,[11] ZnO nanowires,[10] and carbon nanotubes.[9] The field emission studies of these as-grown α-Fe_2O_3 nanostructures were carried out under a two-parallel-plate setup with a 100 or 200 μm gap between the two electrodes inside a vacuum chamber at a low pressure of about 5×10^{-7} Torr. The typical curves of the emission current density as a function of the applied field (J–E plots) from these four samples are shown in Figure 5. The more vertically aligned nanoneedles (sample D) display the best field emission properties, which have the lowest turn-on field (E_{to}, which is defined as the value of E when J reaches 1 μA/cm^2) of 1.7 V/μm, the lowest threshold field (which is defined as the value of E when J becomes 0.1 mA/cm^2) of 2.83 V/μm, and the highest J compared to other samples. At the same time, the
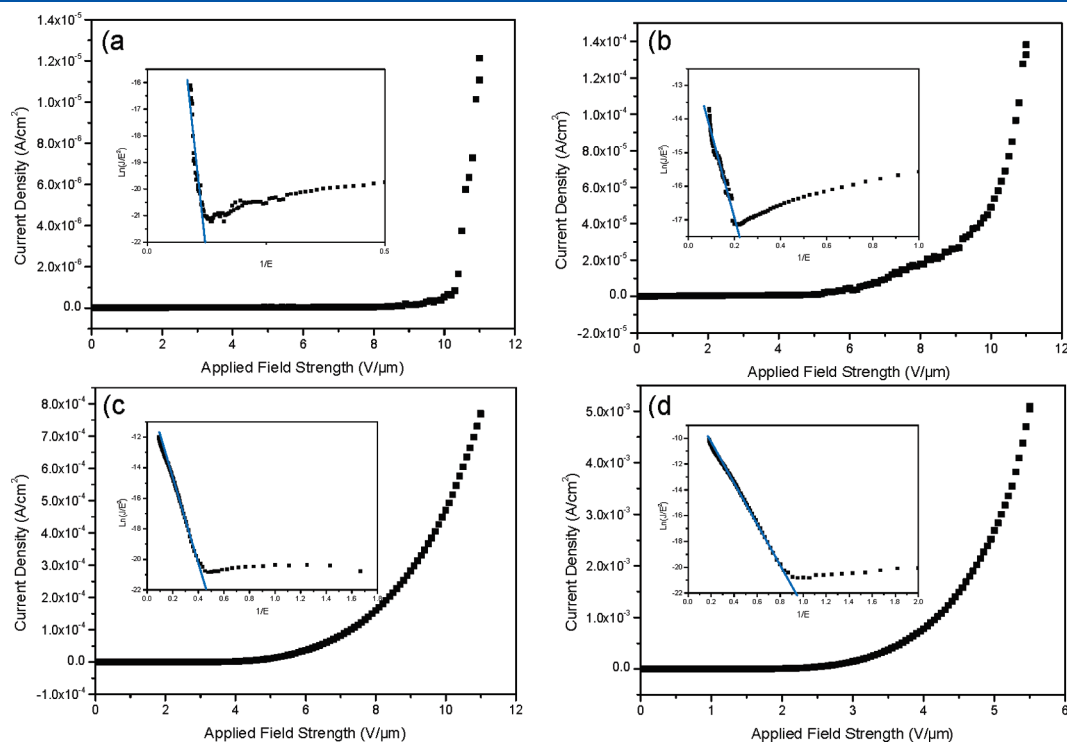

Figure 5. Field emission J–E curves from the four typical morphology α-Fe_2O_3 nanostructure films. (a) sample A, (b) sample B, (c) sample C, (d) sample D. Inserts depict the corresponding FN plots, the linear dependence indicates that the emission satisfies the FN mechanism.

8819

dx.doi.org/10.1021/jp200858g |*J. Phys. Chem. C* 2011, 115, 8816–8824

turn-on fields of other three samples (A, B, and C) are 10.35, 5.05, and 3.75 V/μm and the current density at 11 V/μm are 1.1×10^{-5}, 1.4×10^{-4} and 7.7×10^{-4} A/cm^2, respectively.

The field emission current—voltage characteristics are further analyzed using the Fowler—Nordheim (FN) equation

$$J = \left(\frac{AE^2}{\varphi}\right) \exp\left(-\frac{B\varphi^{3/2}}{E}\right) \qquad (1)$$

or

$$\ln(J/E^2) = \ln(A/\varphi) - B\varphi^{3/2}/E \qquad (2)$$

where A and B are constants of 1.54×10^{-6} AeVV^{-2} and 6.83×10^3 Vμm^{-1}eV$^{-3/2}$, respectively; J is the current density (Acm^{-2}); φ is work function of the materials, which is 5.4 eV for α-Fe$_2$O$_3$.[36] E is the local field (Vμm^{-1}). For nanomaterials, the local field E is always much larger than the average applied electric field, E_{avg}, and we can define an enhancement factor, β, as

$$E = \beta E_{avg} = \frac{\beta V}{d} \qquad (3)$$

V is the applied voltage and d is the gap distance between the emission surface and the anode (d is 100 or 200 μm in this work). β is a parameter that depends on the morphology of the nanomaterials, crystal structures, tip radius, and the density of the emitting points.[26] Some of these parameters of these four samples are listed in Table 1.

We can define an average effective emission area, α, through the equation

$$J = \frac{I}{\alpha} \qquad (4)$$

I is the measured current.

Introduce eqs 3 and 4 into eq 1, and the equation can be expressed as

$$I = \frac{\alpha A(\beta E_{avg})^2}{\varphi} \exp\left(-\frac{B\varphi^{3/2}}{\beta E_{avg}}\right) \qquad (5)$$

The inserts of Figure 5 show the FN plots of these samples. The linear relationship between $\ln(J/E^2)$ and $(1/E)$ indicates that the electron emission from α-Fe$_2$O$_3$ nanostructures follow the Fowler—Nordheim behavior. The slope of $\ln(J/E^2)$ versus $1/E$ plots can be expressed as

$$S = -6.83 \times 10^3 \frac{\varphi^{3/2}}{\beta} \qquad (6)$$

The calculated enhancement factors of these four samples from the FN plots are also listed in Table 1. The quasi-aligned nanoneedles (sample D) possessed the highest β value of 5310, compared to that of sample A, 537; sample B, 4774; and sample C, 3292. The findings that sample D exhibited excellent field emission performance and high β value are likely due to the larger aspect ratio (summarized in Table 1), sharper tips than those of samples A, B, and C and more vertical alignment of its nanostructures. Sample B also possessed a relatively high β value due to lower emitters density which reduces the screening effect. As a comparison, the enhancement factor value, β of sample D is larger than that of vertically aligned CdS nanowires grown on Si substrate ($\beta = 555$),[30] NiSi nanorods ($\beta = 630$),[37] well aligned nanowire CuO arrays ($\beta = 1570$ and 670),[11] and ZnS nanowire

arrays on Si ($\beta = 2700$)[38] and on Cu substrate ($\beta = 3400$).[12] It is even comparable to aligned multiwall carbon nanotube ($\beta = 8400$),[39] which indicates the excellent field emission performance of the as-grown α-Fe$_2$O$_3$ nanoneedles.

The low turn-on field value and high field enhancement indicate that the more vertical nanoneedles (sample D) have a good potential as an excellent field emitter. Through the comparison of the field emission performance of different morphologies α-Fe$_2$O$_3$ nanostuctures, we can summarize that special vertical geometry, high aspect ratio, and good crystallinity are important factors for effective field emission.

Field emission is strongly affected by gas adsorption.[32] Some adsorbed gas molecules can be desorbed through Joule heating, electron emission or ion impact. In this work, we have shown that sample D was the best candidate as FE emitter. Therefore, this sample was selected for the study of residual gas effect on FE characteristic. Similarly, the measurements of field emission properties of 1D well-aligned α-Fe$_2$O$_3$ nanoneedle arrays were conducted using the same two-parallel-plate setup.[11] All of the measurements were carried out at the same parameters described above.

Part a of Figure 6 shows the typical curve of current density as a function of the electric field (J—E) of the as-prepared α-Fe$_2$O$_3$ nanoneedles. It can be seen that the turn-on field is 2.3 V/μm and the current density is 1.39×10^{-4} A/cm^2 at 5.5 V/μm. All of the values are much smaller than those reported in part d of Figure 5 for the same sample. That is attributed to the effect of the adsorbed molecules. We shall elaborate in more details in the following section.

During our experiment, we made an interesting discovery upon chance that the current density kept increasing from quite a low value to a maximum value when we repeatedly ramped voltage from 0 to 1100 V many times under the same conditions. Part b of Figure 6 shows the J—E plots of the α-Fe$_2$O$_3$ nanoneedles corresponding to the repeated voltage ramps. As evident from these curves, initially, the current density was only 1.39×10^{-4} A/cm^2 when the applied field reached a value of 5.5 Vμm^{-1}, and the turn-on field was as high as 2.3 Vμm^{-1}, which was the same as the curve of part a of Figure 6. However, by just ramping the applied electric field a second time without changing the parameters, the current density rose a bit to 2.5×10^{-4} A/cm^2 at the same value of E. And the more we repeated the voltage ramping, the higher the measured current density. After 40 repeated voltage ramps, the current density reached an ultralarge value of about 5.1×10^{-3} A/cm^2 at the same E value, and the turn-on field decreased to 1.7 Vμm^{-1}, which are essentially the results shown in part d of Figure 5. Similarly, the curves shown in parts a—c of Figure 5 were obtained using the same treatment, namely, repeating the voltage ramping many times. If we kept repeating this process, the current density would rise to a maximum value of about 1.1×10^{-3} A/cm^2. The J—E plot is shown in part c of Figure 6. That means the current density increased about 100 times just by repeated voltage ramp without changing any other parameters. The current density at the same E value of 5.5 Vμm^{-1} versus voltage ramps number is shown in part d of Figure 6. We see that the current density became saturated after sufficient number of voltage ramps.

The reasons of this phenomenon are closely related to the working principle of most semiconductor oxide gas sensors.[40] When α-Fe$_2$O$_3$ nanoneedles is exposed to air, the oxygen molecules adsorb on the surface of the nanoneedles and form O_2^- or O_2^{2-} ions by capturing electrons from the conductance band of α-Fe$_2$O$_3$ nanoneedles. So these α-Fe$_2$O$_3$ nanoneedles have a

8820

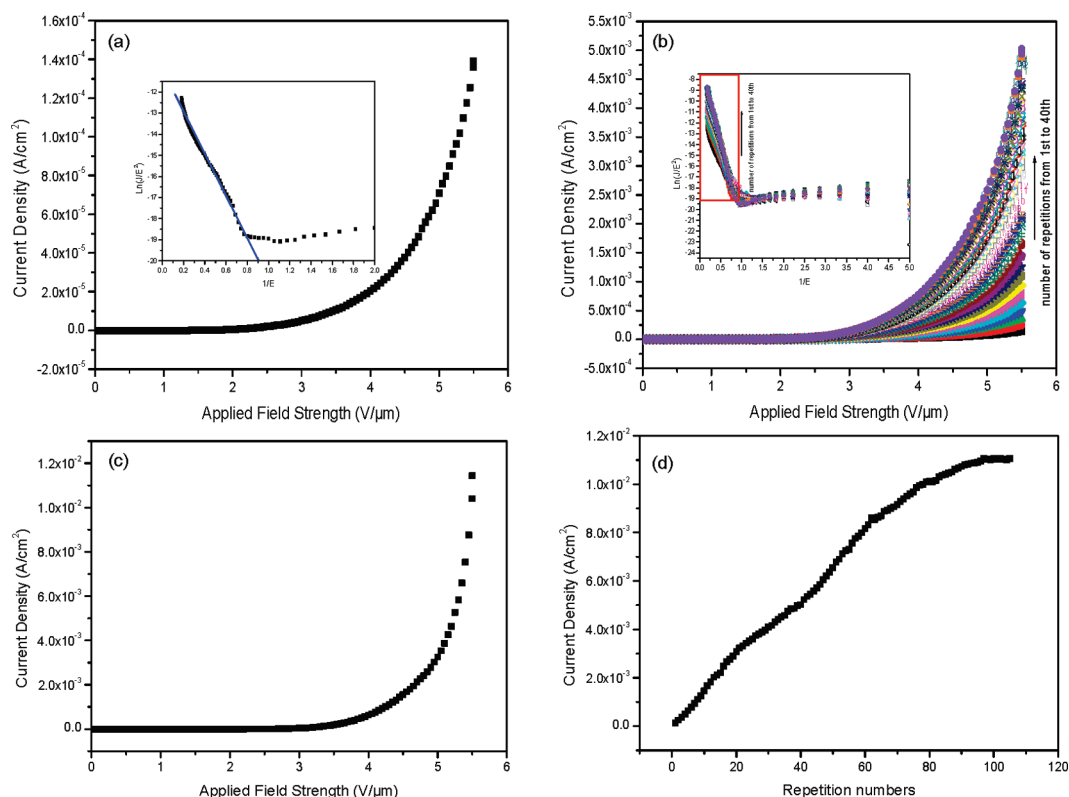dx.doi.org/10.1021/jp200858g |*J. Phys. Chem. C* 2011, 115, 8816–8824

Figure 6. Typical $J-E$ curves of sample D carried out (a) 1st voltage ramp; (b) 40th voltage ramp, inserts are the corresponding FN plots; (c) repeated to a maximum value; (d) current density varies with the repetition numbers at the same E value of 5.5 Vμm^{-1}.

higher resistance under air ambient, which can deeply influence the performance of field emitter. Inside a high vacuum chamber, with only the help of vacuum pump, it is not sufficient to remove the oxygen molecules adsorbed on the α-Fe$_2$O$_3$ nanoneedles surface. In reality, the α-Fe$_2$O$_3$ nanoneedles are not defect-free. Electrons that flow along nanoneedles could be scattered by defects and generate Joule heating. When a high electric field is applied to these nanoneedles, the nanoneedles without or with less adsorbed oxygen molecules will allow electrons to flow along and thus give rise to Joule heating. The heated nanoneedles could desorb the oxygen gas molecules and lower the concentration of O_2^- or O_2^{2-} ions on the surface of the nanoneedles. Heat energy could be spread from the heated nanoneedles to the neighboring nanoneedles, causing the O_2^- or O_2^{2-} ions on these nanoneedles to desorb and hence making them field emission active as well. Hence, with prolonged field emission experiment, the conductivity of the α-Fe$_2$O$_3$ nanoneedles increased and this could improve their field emission performance. Parts a−d of Figure 7 show the schematic diagram of oxygen molecules desorption during the prolonged field emission process.

Because our ITO electrode was coated with a layer of phosphor, we could identify the field emitting region during our experiment. Parts a−c of Figure 8 show the fluorescent FE images obtained at the 1st, 20th, and 40th voltage ramp respectively under an applied voltage of 1000 V. We can see from part a of Figure 8 that, initially, only the nanoneedles inside the white circle lines were emitting electrons. That means less molecules were adsorbed on the surface of these nanoneedles. The Joule heat created inside these nanoneedles could spread to the nearest neighbor, as shown in parts b and c of Figure 7.
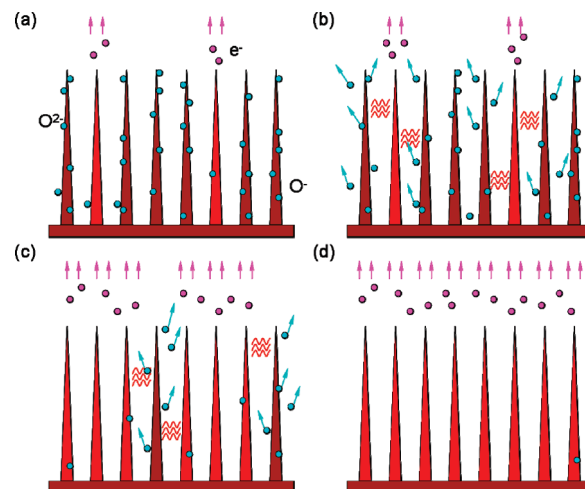

Figure 7. Schematic diagram of oxygen molecules desorption during the prolonged FE process.

Therefore, nanoneedles closest to those which are emitting electrons could capture the heat energy and these in turn would have their surface molecules desorbed and then take part in the field emission. As shown in part b of Figure 8, the nanoneedles near the original emission sites became activated for field emission and the emission area increased gradually. After suffi-cient repetition, most of the adsorbed molecules were removed and all of the nanoneedles could emit electron, the whole area became active emitters with high brightness in the fluorescent
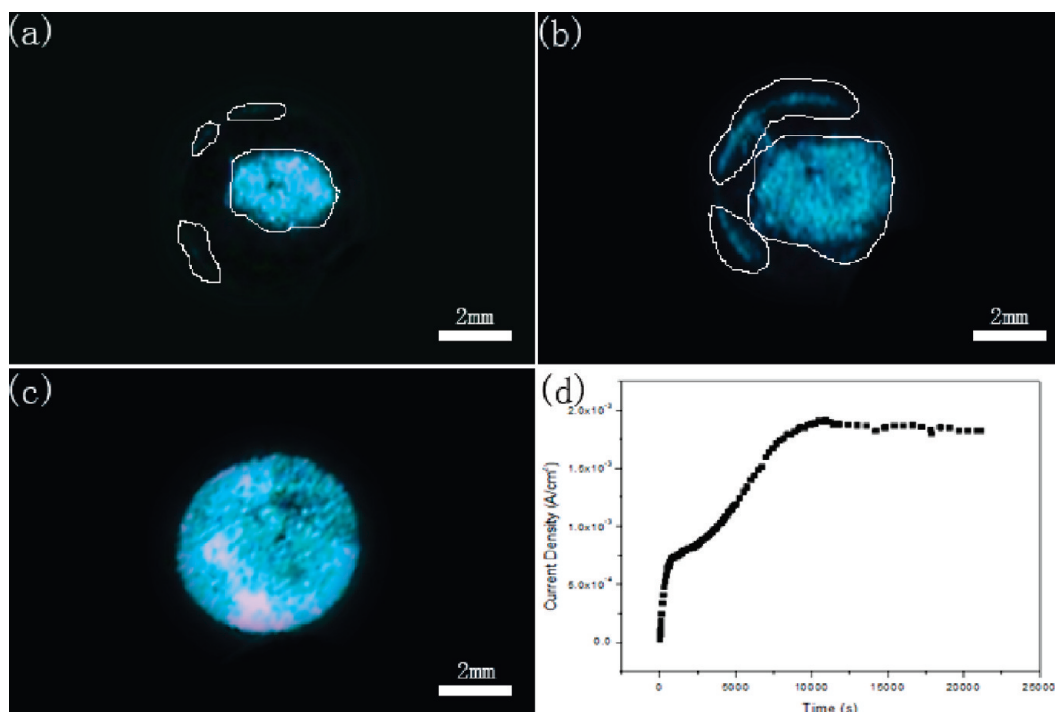
Figure 8. Fluorescence of field emission images of α-Fe$_2$O$_3$ nanoneedle arrays (sample D): (a) 1st voltage ramp, (b) 20th voltage ramp, (c) 40th voltage ramp. The white circle lines representing the emission area became lager with the replication numbers increase. (d) Current density variation with increasing time applied field strength kept at 4.5 V/μm.

image, which is shown in part c of Figure 8. The dynamic process of the current density changes as a function of time was recorded as a curve shown in part d of Figure 8. The applied field strength was kept at 4.5 Vμm^{-1} for 6 h. Evidently, the dynamic process of the increment in current density can be divided into three main segments, the rapidly increasing state, gradually increasing state and finally a stable field emission state. This indicates the adsorbed oxygen molecules desorb at a rate from fast to slow until the desorption ceased.

To further investigate this phenomenon, different gases were introduced into the vacuum chamber for a few minutes and then these gases were pumped out; and the effects caused by these gases on the FE properties of α-Fe$_2$O$_3$ nanoneedles were studied. At first, we repeatedly (about 60 times) ramped the applied voltage to 1100 V under high vacuum until the measured current density reached a very high value. The $J-E$ plot is shown in part a of Figure 9. Then we introduced air into the chamber until the pressure raised to atmospheric condition and maintained at this condition for about 10 min. After that we pumped down the chamber to 5 × 10^{-7} Torr again. At this point, the FE measurement commenced with the usual voltage ramp. When the 1100 V voltage was applied at this condition, the measured current density decreased to the original low value 2.2 × 10^{-4} A/cm^2, as shown in part c of Figure 9. However, in a similar experiment, if the gas introduced into the chamber was nitrogen instead of air, the measured current density would still be a very high value, 7.9 × 10^{-3} A/cm^2, as can be seen from part b of Figure 9. From this experiment, it was clear that the gas molecule that most influenced the field emission property is oxygen molecule or water adsorbed on the materials surface. The third time, simulated air (without water), which is composed of 79% nitrogen and 21% oxygen, was introduced into the chamber and maintained at the
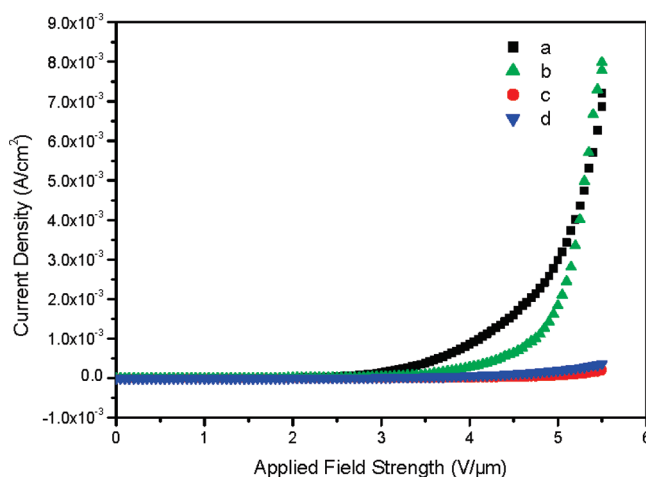

Figure 9. Typical $J-E$ curve of sample D obtained (a) after repeated voltage ramp and before the introduction of air/N$_2$, (b) after the introduction and removal of N$_2$, (c) after the introduction and removal of air, and (d) after the introduction and removal of simulated air.

atmospheric condition for 10 min. Then the chamber was pumped down to high vacuum and applied the electric field again. The corresponding $J-E$ plot is shown in part d of Figure 9. As shown, the current density also decreased to a very low value. This suggests that oxygen adsorption caused the great decrease in the current density. The similar phenomena were also observed from other three samples but to a lesser degree. That is attributed to the fact that the α-Fe$_2$O$_3$ nanoneedles have larger surface to volume ratio and can adsorb more oxygen molecules on the surface than other three samples.

The insert of part b of Figure 6 shows the FN plots corresponded to the reiteration numbers. Inside the red rectangle, the absolute values of the slopes increase with number of the replications. Therefore, the corresponding values of β decrease from 8481 (first time, insert of part a of Figure 6) to 5310 (40th time). The reduction was attributed to screening effect with the emitter density increasing. Considering the screening effect of adjacent emitters, the local electrical field E can be expressed by Filip's model[41]

$$E = \kappa \frac{V}{r} + (1 - \kappa)\frac{V}{d} \qquad (7)$$

where κ is a parameter used for describing the degree of screening effect, which varies from 1 for a single emitter to 0 for extremely densely arranged emitters. And r is the tip radius of the emitter materials. Combining eqs 3 and 7, a formula for estimating the field enhancement factor of the emitter film can be derived as[42]

$$\beta = 1 + \kappa \left(\frac{d}{r} - 1\right) \cong 1 + \kappa \frac{d}{r} \qquad (8)$$

We can define an absolute enhancement factor, β_0, expressed as,

$$\beta_0 = 1 + \frac{d}{r} \cong \frac{d}{r} \qquad (9)$$

which implies no screening effect case, namely, κ equals to 1. Combining eqs 8 and 9, β can be expressed as

$$\beta \cong \kappa\beta_0 \qquad (10)$$

Therefore, κ also can act as a correction factor for screening effect. Substituting the d value used in our experiment and the average r value of sample D (from part c of Figure 4) to eq 9, the absolute enhancement factor for a single α-Fe_2O_3 nanoneedle can be calculated as high as 2×10^4, indicating that the local electric field at the top tip of the emitter could be sharply enhanced due to the very small radius of curvature of the ultrathin nanotip. For the field emission measured at the 1st and 40th times, using the actual β value of 8481 and 5310 calculated from FN plots, the factor κ is estimated to be 0.42 and 0.27, respectively. Thereby, with the replication numbers increasing, the κ factor decreases due to the higher screening effect, which indicates the screening effect plays an important part in the practical field emission process of 1D nanomaterial arrays. This can also been seen from Figure 8, from a to c, the emitter density rises to cover almost the whole area of the substrate, leading to the domination of the screening effect in the FE process.

4. CONCLUSIONS

In conclusion, quasi-1D α-Fe_2O_3 nanostructure arrays with four kinds of different morphologies were fabricated through simple methods of thermally oxidizing Fe foil. Measurements of their field emission properties show that the more vertically aligned α-Fe_2O_3 nanoneedle arrays produce the higher FE current density and possess the lower turn-on field and larger field-enhancement factor due to the better alignment, higher aspect ratio and very sharp tips. The physisorption effects of oxygen molecules on the nanoneedle surface were also investigated. Current-induced Joule heating can remove the physisorption effects through repeated ramping of the applied electric field. By comparing the emitter density, the decreasing of the field-enhancement factor caused by screening effect was also observed.

This insight can provide a new approach to enhance the field emission performance of quasi-1D nanomaterials. The experimental results are expected to shed some light on fundamental physical and chemical processes of how oxygen molecules adsorption affects the field emission properties of the 1D nanomaterials, as well as applied interests alike.

■ ASSOCIATED CONTENT

ⓢ Supporting Information. SEM images of iron foil heated at 500 and 600 °C for 4 h, Raman spectra and XRD pattern characterization of these samples. This material is available free of charge via the Internet at http://pubs.acs.org.

■ AUTHOR INFORMATION

Corresponding Author
*E-mail: physowch@nus.edu.sg.

■ REFERENCES

(1) Ohno., H. *Science* **1998**, *281*, 951–956.
(2) Zeng, H. B.; Cai, W. P.; Liu, P. S.; Xu, X. X.; Zhou, H. J.; Kingshirn, C.; Kalt, H. *ACS Nano* **2008**, *2*, 1661–1670.
(3) Yuan, G. D.; Zhang, W. J.; Jie, J. S.; Fan, X.; Zapien, J. A.; Leung, Y. H.; Luo, L. B.; Wang, P. F.; Lee, C. S.; Lee, S. T. *Nano Lett.* **2008**, *8*, 2591–2597.
(4) Song, J. F.; Bird, J. P.; Ochiai, Y. *J. Phys.: Condens. Matter* **2005**, *17*, 5263–5268.
(5) Law, M.; Greene, L. E.; Johnson, J. C.; Saykally, R.; Yang, P. D. *Nat. Mater.* **2005**, *4*, 455–459.
(6) Wang, Z. L.; Song, J. H. *Science* **2006**, *312*, 242–246.
(7) Wang, X. D.; Song, J. H.; Liu, J.; Wang, Z. L. *Science* **2007**, *316*, 102–105.
(8) Saito, Y.; Uemura, S. *Carbon* **2000**, *38*, 169–182.
(9) Baughman, R. H.; Zrkhidov, A. A.; de Heer, W. A. *Science* **2002**, *297*, 787–792.
(10) Banerjee, D.; Jo, S. H.; Ren, Z. F. *Adv. Mater.* **2004**, *16*, 2020–2032.
(11) Zhu, Y. W.; Yu, T.; Cheong, F. C.; Xu, X. J.; Lim, C. T.; Tan, V. B. C.; Thong, J. T. L.; Sow, C. H. *Nanotechnology* **2005**, *16*, 88–92.
(12) Liu, B. D.; Bando, Y.; Jiang, X.; Li, C.; Fang, X. S.; Zeng, H. B.; Terao, T.; Tang, C. C.; Mitome, M.; Golberg, D. *Nanotechnology* **2010**, *21*, 375601.
(13) Xu, N. S.; Huq, S. E. *Mater. Sci. Eng. Res.* **2005**, *48*, 47–189.
(14) Shi, X. L.; Cao, M. S.; Yuan, J.; Zhao, Quan. Liang.; Kang, Y. Q.; Fang, X. Y.; Chen, Y. J. *Appl. Phys. Lett.* **2008**, *93*, 183118.
(15) Chen, Y. J.; Zhu, C. L.; Wang, L. J.; Gao, P.; Cao, M. S.; Shi, X. L. *Nanotechnology* **2009**, *20*, 045502.
(16) Zhu, C. L.; Chen, Y. J.; Wang, R. X.; Wang, L. J.; Cao, M. S.; Shi, X. L. *Sens. Actuators, B* **2009**, *140*, 185–189.
(17) Lin, Y.; Sun, F. Q.; Yuan, X. Y.; Geng, B. Y.; Zhang, L. D. *Appl. Phys. A: Mater. Sci. Process.* **2004**, *78*, 1197–1199.
(18) Jin, J.; Ohkoshi, S.; Hashimoto, K. *Adv. Mater.* **2004**, *16*, 48–51.
(19) Vayssieres, L.; Sathe, C.; Butorin, S. M.; Shuh, D. K.; Nordgren, J.; Guo, J. *Adv. Mater.* **2005**, *17*, 2320–2323.
(20) Fu, Y.; Chen, J.; Zhang, H. *Chem. Phys. Lett.* **2001**, *350*, 491–494.
(21) Fu, Y. Y.; Wang, R. M.; Xu, J.; Chen, J.; Yan, Y.; Narlikar, A. V.; Zhang, H. *Chem. Phys. Lett.* **2003**, *379*, 373–379.
(22) Hsu, L. C.; Li, Y. Y.; Hsiao, C. Y. *Nanoscale Res. Lett.* **2008**, *3*, 330–337.
(23) Yu, T.; Zhu, Y. W.; Xu, X. J.; Yeong, K. S.; Shen, Z. X.; Chen, P.; Lim, C. T.; Thong, J. T. L.; Sow, C. H. *Small* **2006**, *2*, 80–84.
(24) Zhu, Y. W.; Yu, T.; Sow, C. H.; Liu, Y. J.; Wee, A. T. S.; Xu, X. J.; Lim, C. T.; Thong, J. T. L. *Appl. Phys. Lett.* **2005**, *87*, 023103.
(25) Wu, J. Q.; Chen, Jun; Deng, S. Z.; Xu, N. S. *J. Vac. Sci. Technol., B* **2010**, *28*, C2B34–C2B37.

8823

dx.doi.org/10.1021/jp200858g |*J. Phys. Chem. C* 2011, 115, 8816–8824

(26) Gautam, U. K.; Fang, X. S.; Bando, Y.; Zhan, J. H.; Golberg, D. *ACS Nano* **2008**, *2*, 1015–1021.

(27) Zhao, Q.; Feng, S. Q.; Zhu, Y. W.; Xu, X. Y.; Zhang, X. Z.; Song, X. F.; Xu, J.; Chen, L.; Yu, D. P. *Nanotechnology* **2006**, *17*, S351–S354.

(28) Rakhi, R. B.; Lim, X.; Gao, X.; Wang, Y.; Wee, A. T. S.; Sethupathi, K.; Ramaprabhu, S.; Sow, C. H. *Appl. Phys. A: Mater. Sci. Process.* **2010**, *98*, 195–202.

(29) Pan, L. J.; Konishi, Y.; Tanaka, H.; Suekane, O; Nosaka, T.; Nakayama, Y.; Jpn., J. *Appl. Phys.* **2005**, *44*, 1652–1654.

(30) Zhai, T.; Fang, X.; Bando, Y.; Liao, Q.; Xu, X.; Zeng, H.; Ma, Y.; Yao, J.; Golberg, D. *ACS Nano* **2009**, *3*, 949–959.

(31) Chernozatonskii, L. A.; Kosakovskaya, Z. Y.; Gulyaev, Y. V.; Sinitsyn, N. I.; Torgashov, G. V.; Zakharchenko, Y. F. *J. Vac. Sci. Technol., B* **1996**, *14*, 2080–2082.

(32) Chen, C. W.; Lee, M. H.; Clark, S. J. *Diamond Relat. Mater.* **2004**, *13*, 1306–1313.

(33) Cvelbar, U.; Chen, Z.; Sunkara, M. K.; Mozetic, M. *Small* **2008**, *4*, 1610–1614.

(34) Chourpa, I.; Douziech-Eyrolles, L.; Ngaboni-Okassa, L.; Fouquenet, J. F.; Cohen-Jonathan, S.; Souce, M.; Marchais, H.; Dubois, P. *Analyst* **2005**, *130*, 1395–1403.

(35) Beattie, I. R.; Gilson, T. R. *J. Chem. Soc. A* **1970**, *6*, 980–986.

(36) Hendrich, V. E.; Cox, P. A. *The Surface Science of Metal Oxides*; Cambridge University Press: Cambridge, U.K., 1994.

(37) Ok, Y. W.; Seong, T. Y.; Choi, C. J.; Tu, K. N. *Appl. Phys. Lett.* **2006**, *88*, 043106.

(38) Chen, Z. G.; Cheng, L.; Zou, J.; Yao, X. D.; Lu, G. Q.; Cheng, H. M. *Nanotechnology* **2010**, *21*, 065701.

(39) Seelaboyina, R.; Boddepalli, S.; Noh, K.; Jeon, M.; Choi, W. *Nanotechnology* **2008**, *19*, 065605.

(40) Wan, Q.; Li, Q. H.; Chen, Y. J.; Wang, T. H.; He, X. L.; Li, J. P.; Lin, C. L. *Appl. Phys. Lett.* **2004**, *84*, 3654–3656.

(41) Filip, V.; Nicolaescu, D.; Tanemura, M.; Okuyama, F. *Ultramicroscopy* **2001**, *89*, 39–49.

(42) Zhao, Q.; Xu, J.; Xu, X. Y.; Wang, Z.; Yu, D. P. *Appl. Phys. Lett.* **2004**, *85*, 5331–5333.